

# Disk stability and neutral hydrogen as a tracer of dark matter

Gerhardt R. Meurer<sup>1</sup>, Zheng Zheng<sup>2</sup>, and W.J.G. de Blok<sup>3,4</sup>

<sup>1</sup>*International Centre for Radio Astronomy Research, The University of Western Australia, 35 Stirling Highway, Crawley, WA 6009, Australia*

<sup>2</sup>*The Johns Hopkins University, Department of Physics and Astronomy, Baltimore, MD 21218, U.S.A.*

<sup>3</sup>*Netherlands Institute for Radio Astronomy (ASTRON), Postbus 2, 7990 AA Dwingeloo, the Netherlands*

<sup>4</sup>*ACGC, Dept of Astronomy, University of Cape Town, Private Bag X3, Rondebosch 7700, South Africa*

MNRAS accepted (arXiv version 3), 21 Dec, 2012

## ABSTRACT

We derive the projected surface mass distribution  $\Sigma_M$  for spherically symmetric mass distributions having an arbitrary rotation curve. For a galaxy with a flat rotation curve and an ISM disk having a constant Toomre stability parameter,  $Q$ , the ISM surface mass density  $\Sigma_g$  as well as  $\Sigma_M$  both fall off as  $R^{-1}$ . We use published data on a sample of 20 well studied galaxies to show that ISM disks do maintain a constant  $Q$  over radii usually encompassing more than 50% of the H I mass. The power law slope in  $\Sigma_g$  covers a range of exponents and is well correlated with the slope in the epicyclic frequency. This implies that the ISM disk is responding to the potential, and hence that secular evolution is important for setting the structure of ISM disks. We show that the gas to total mass ratio should be anti-correlated with the maximum rotational velocity, and that the sample falls on the expected relationship. A very steep fall off in  $\Sigma_g$  is required at the outermost radii to keep the mass and angular momentum content finite for typical rotation curve shapes, and is observed. The observation that H I traces dark matter over a significant range of radii in galaxies is thus due to the disks stabilising themselves in a normal dark matter dominated potential. This explanation is consistent with the cold dark matter paradigm.

**Key words:** galaxies: structure – galaxies: evolution – galaxies: spiral – galaxies: irregular – dark matter.

## 1 INTRODUCTION

H I has long been the best tracer of Dark Matter (DM) in galaxies (e.g. Bosma 1981; van der Hulst et al. 1993). This is because it typically extends much further than the optically bright portion of a galaxy, in a fairly regular disk. But this ability to trace DM seems uncanny: typically the projected DM surface density scales very well with the measured H I surface density (Bosma 1981; Sancisi 1983; Carignan & Beaulieu 1989; Carignan et al. 1990; Carignan & Puche 1990a,b; Jobin & Carignan 1990; Broeils 1992; Meurer et al. 1996; Hoekstra et al. 2001). Mestel (1963) had already shown that the flat rotation curve typically seen in the outer parts of spiral galaxies requires a surface mass density  $\Sigma(R) \propto R^{-1}$  fall-off in the disk, if that is where the dominant mass is located. This is not what is observed in the optical but close to the behaviour of H I disks. H I not only is a good dynamical tracer of DM but its distribution scales linearly with the DM in the outskirts of galaxies. This has prompted some researchers to posit that DM may be gaseous, perhaps in a disk

configuration (Pfenniger et al. 1994; Pfenniger & Combes 1994; Gerhard & Silk 1996; Pfenniger & Revaz 2005; Bournaud et al. 2007; Hessman & Ziebart 2011). The scaling between DM and H I is also well explained by the Modified Newtonian Dynamics (MOND) hypothesis in which the gravitational force law is modified; in a MOND analysis, H I is the only significant mass in the outskirts of galaxies (e.g. Sanders & McGaugh 2002). Either explanation poses a problem for the standard Cold Dark Matter (CDM) scenario. A gaseous form of baryonic DM would be dissipative, whereas in the CDM scenario DM only interacts via gravity and so is non-dissipative. The MOND scenario requires no DM.

We propose an explanation for the linear scaling between H I and DM that is consistent with the CDM scenario. The ISM distribution in disks is configured to maintain a uniform minimum stability over as much of the disk as possible. For a flat rotation curve, this will result in a surface density profile having the same form as the dominant mass. In § 2 we give the basis of our model. In § 3 we gather

recent H I rotation curve (RC) data to test this hypothesis. § 4 discusses our results and presents our conclusions.

## 2 THE STRUCTURE OF DYNAMICALLY STABLE GAS DOMINATED DISKS

The stability of a purely stellar or purely gaseous disk is a well studied problem starting with the work of Safronov (1960) and Toomre (1964). For a disk to be stable against axi-symmetric perturbations, the support from a combination of random motions and centrifugal forces must be larger than the gravitational attraction. This is expressed as a ratio, the “Toomre  $Q$ ” parameter:

$$Q \equiv \frac{\sigma \kappa}{\pi G \Sigma} \quad (1)$$

where  $\Sigma$  is the mass density in the disk,  $\sigma$  is the velocity dispersion, and  $\kappa$  is the epicyclic frequency given by

$$\kappa = \frac{V}{R} \sqrt{2 \left( 1 + \frac{R}{V} \frac{dV}{dR} \right)} \quad (2)$$

with  $V$  being the rotational velocity at radius  $R$ . For a purely gaseous disk to be stable  $Q > 1$ , while a purely stellar disk requires  $Q > 1.07 = 3.36/\pi$  for stability. Unstable disks result in the formation of bars and spiral arms which gather the ISM, enhancing star formation efficiency and thus reheating the disk through feedback (Hohl 1971; Sellwood & Carlberg 1984; Debattista et al. 2006). The stability of a multi-component disk, i.e. gas and stars, is more complex (Jog & Solomon 1984; Rafikov 2001; Romeo & Wiegert 2011). Here we are concerned primarily with the outer disk, where the ISM mass dominates. In those cases the single fluid  $Q$  given by eq. 1 is sufficient for our purposes. In some of the galaxies we analyse the stellar disk *is* important, and we show that the results are usually not significantly different over the radii we are concerned with when a multi-component disk analysis is employed.

As done commonly, we consider a galaxy where the dominant mass has a spherical distribution of mass with density  $\rho_M(R)$ , which also contains an embedded “light” (low mass) gas disk having surface mass density  $\Sigma_g$ . We take the projected *total* surface mass density  $\Sigma_M(R)$  to be

$$\Sigma_M(R) = 2R\rho_M(R). \quad (3)$$

This is the projection of a spherical shell onto a ring of the same radius at the equator. This is the correct definition when we are concerned with the rotation curve (hereafter RC, or  $V$ ) of the dominant mass. Under our assumptions, disk particles in circular orbits only feel the potential of the mass interior to their orbit. We assume this geometry precisely because it allows some simple derivations. Olling & Merrifield (2000) note that theory indicates that DM halos should be somewhat flattened spheroids, but that the limited observations do not clearly state what the flattening typically is. If the DM is in a disk, as might be expected for gaseous form of DM, then the spherical approximation does not hold. As can be discerned from Fig. 1 of Hessman & Ziebart (2011), assuming a spherical geometry will cause us to underestimate  $\Sigma_M(R)$  at large  $R$  in this case. However, for typically assumed RC shapes and beyond a few core radii, the ratio of true to inferred  $\Sigma_M(R)$  changes slowly

and only by  $\sim 10\%$ . Hence the simplifying assumption of a spherical halo is not critical to our results.

Assuming standard Newtonian gravity and pure circular orbits, it is straight-forward to derive  $\Sigma_M(R)$  as a function of the RC

$$\Sigma_M = \frac{1}{2\pi G R} \frac{d(RV^2)}{dR} \quad (4)$$

which becomes

$$\Sigma_M = \frac{1}{2\pi G R} \left( 2R \frac{dV}{dR} + V^2 \right). \quad (5)$$

We define  $\zeta$  to be the local gas to total mass ratio

$$\zeta \equiv \frac{\Sigma_g}{\Sigma_M}. \quad (6)$$

The case of  $\zeta$  being constant corresponds to the gas disc tracing the total mass. We will also have occasion to consider the integrated quantity

$$\mathcal{Z} = \frac{M_g}{M(R_{\max})} \quad (7)$$

where  $M(R_{\max})$  is the mass within the maximum radius,  $R_{\max}$ , of the H I distribution.

We emphasise that the mass densities  $\Sigma_M$ , and  $\rho_M$  in eq. 3 and throughout are the projected and spherically averaged mass densities of *all* mass, i.e. disk (stars and gas), bulge, and halo (luminous and dark). Likewise  $\zeta$  and  $\mathcal{Z}$  are the local and integrated gas to *total* mass ratio. We adopt these definitions to simplify the analysis, avoiding the need to fit the rotation curve into contributions from the different components. The quantity  $\zeta$  is thus the reciprocal of the ratio plotted in Fig. 7 of Bosma (1981) where it first became apparent that H I traces whatever dominates the mass in the outskirts of galaxies. The implications of our results stem from the well established result that at large radius the dominant form of mass in galaxies is DM (e.g. Freeman 1970; Rubin et al. 1978; Faber & Gallagher 1979; Kent 1987; Carignan & Beaulieu 1989; Carignan et al. 1990; de Blok et al. 2008).

Solving eq. 1 for  $\Sigma_g$  and employing eq. 2 and eq. 5 yields

$$\zeta = \frac{2\sigma}{Q} \frac{\sqrt{2[1 + (R/V)(dV/dR)]}}{V + 2R(dV/dR)}. \quad (8)$$

It is instructive to adopt a power law form to the RC

$$V \approx kR^\gamma, \quad (9)$$

where  $k$  is a constant. This approximation works fairly well over a limited range of radii in galaxies, which is sufficient for our purposes. This results in

$$\zeta = \frac{\sigma}{Q} \frac{\sqrt{8(1+\gamma)}}{kR^\gamma(2\gamma+1)}. \quad (10)$$

The power law index  $\gamma$  has a narrow range of allowed values:

$$-\frac{1}{2} \leq \gamma \leq 1. \quad (11)$$

A  $\gamma$  below this range means the RC drops faster than Keplerian, while  $\gamma$  above this range requires a “hollow” mass distribution.  $\gamma = -1/2$  corresponds to  $\zeta = \infty$  since this requires  $\Sigma_M = 0$ . In the outer disks of many disk galaxies the RC is flat at its maximum value, hence  $\gamma = 0$ ,  $V = V_{\max}$ , and thus

$$\zeta = \frac{\sqrt{8}}{V_{\max}} \frac{\sigma}{Q}. \quad (12)$$

If  $\sigma$  and  $Q$  are also constant, or their ratio is, then  $\zeta$  is also constant and the gas disk will track the total mass distribution. From eq. 5 then

$$\Sigma_M(R) = \frac{1}{2\pi G} \frac{V_{\max}^2}{R}, \quad \Sigma_g(R) = \frac{\sqrt{2}\sigma}{\pi Q G} \frac{V_{\max}}{R}. \quad (13)$$

This is the well known relationship of the total surface mass density falling off as  $R^{-1}$  where the RC is flat, which is a fair approximation of what is observed in most spiral galaxies.

We posit that disks evolve towards maintaining a constant  $Q$ . Simple feedback should encourage such a condition. Over the optical face of a galaxy, star formation is likely to be the regulating agent. Regions of the disk where  $Q$  is higher than average have a disk that is a combination of hot or under-dense compared to their surroundings. In these regions any star formation activity would decrease (relative to their surroundings), lowering  $\sigma$ , thus allowing more ISM to accumulate or cool and decreasing  $Q$ . In regions where  $Q$  is low, the disk is a combination of cold or over-dense. Star formation will be enhanced in these areas, increasing  $\sigma$  as feedback from the newly born stars kicks in. While the outer disk is usually considered to be devoid of star formation, the discovery of outlying H II regions (Ferguson et al. 1998) and XUV disks (Thilker et al. 2005, 2007) indicates that in many cases there are sources of new stars that can help regulate disks. Even in the case of pure gaseous disks, the simulations by Wada et al. (2002) show that a turbulent clumpy disk develops with a large range of  $Q$  over short scales, but with a quasi-steady equilibrium maintained with little variation in average  $Q$  with time or radius.

### 3 OUTER DISK Q MEASUREMENTS

We gathered data on 20 galaxies to test our hypothesis that outer disks maintain a nearly constant  $Q$ . The majority of the data is from *The H I Nearby Galaxy Survey* (THINGS) for which detailed published RCs can be found in Oh et al. (2008) and de Blok et al. (2008). Data from individual studies of six additional galaxies with extended disks are included to test the robustness of the results (Cannon et al. 2009; Elson et al. 2010; Gentile et al. 2007; Struve et al. 2010; Warren et al. 2004; Westmeier et al. 2011). The main criteria for selection is that the galaxy have tabulated data available from recent studies (within  $\sim 5$  years) and H I profiles extending beyond the optical radius  $R_{25}$  (where the  $B$  band surface brightness is 25 mag arcsec $^{-2}$ ). Table 1 lists basic quantities of the sample and the data sources, arranged by the maximum rotational velocity  $V_{\max}$ . This sample covers  $50 \text{ km s}^{-1} \lesssim V_{\max} \lesssim 375 \text{ km s}^{-1}$  and the full range of late-type galaxy morphologies including spirals from types S0 (NGC 1167) to Sd (e.g. NGC 300), irregulars of types Sm (IC 2574) and Im (e.g. NGC 3741) as well as Blue Compact Dwarf (BCD) galaxies (e.g. NGC 2915). The majority of the sample is nearby, with only two having distance  $D > 15$  Mpc. Therefore, we adopt  $D$  values that are not based on the Hubble flow, where possible. The sources of  $D$  are given in Table 1. For the two cases where we use  $D$  based on

redshift, we adopt the model given by NED<sup>1</sup> for the Hubble flow corrected for inflow to the Virgo cluster, Great Attractor, and Shapley super-cluster (Mould et al. 2000) and standard cosmological parameters  $H_0 = 73 \text{ km s}^{-1} \text{ Mpc}^{-1}$ ,  $\Omega_{\text{matter}} = 0.27$ , and  $\Omega_{\text{vacuum}} = 0.73$ .

The main observational quantities of importance are the RC and the  $\Sigma_g$  profile. The RCs are shown in Fig. 1. We fit a cubic-spline to the RCs using knots set by eye. In performing the fit, we keep the number of spline knots to a minimum and try to follow the data to within the errors. However, we smooth over small scale fluctuations in the RCs, presumably due to spiral arms or non circular motions. The fitted splines are shown as continuous lines in Fig. 1. We chose this functional form for its flexibility and because it allows for easy evaluation of the derivative  $dV/dR$  needed for the calculation of  $\kappa$  and thus  $Q$ . For comparison, we plot a model RC using the functional form adopted by Leroy et al. (2008), with parameters  $V_{\text{flat}} = 150 \text{ km s}^{-1}$ ,  $R_{\text{flat}} = 0.5R_{25}$ , and  $R_{25} = 8 \text{ kpc}$ . The sample includes many galaxies with flat RCs at large radii, like this model (DDO154, ESO215<sup>2</sup>, NGC 2915, NGC 2403, NGC 3198, NGC 6946, NGC 2841), or are still rising (IC 2574, NGC 3741, NGC 3621). However, about half the sample have RCs that have a substantial range of radii where they are declining (NGC 2366, NGC 300, ADBS J1138<sup>3</sup>, NGC 7793, NGC 4736, NGC 5055, NGC 2903, NGC 3521, NGC 3031, NGC 1167). To illustrate the range of shapes, we fit a power-law RC to the data between a limited range of radii, defined below. These and the other power-law fits in this paper were performed as linear fits in log-log space using the IDL procedure MPFIT (Markwardt 2009). The fits are shown as dashed lines in Fig. 1, with the fit parameters, including zeropoint, slope  $\gamma$ , and dispersion of the residuals  $\epsilon$  listed in Table 2.

The  $\Sigma_g$  profiles are shown in Fig. 2. They were derived from the inclination corrected H I profiles assuming  $\Sigma_g = 1.3\Sigma_{\text{HI}}$  to account for elements heavier than hydrogen. Since we are primarily interested in the outer disk we assume that the molecular content is negligible. The profiles are drawn in log-log space, to highlight any power-law behaviour. In general, the profiles are nearly flat or decreasing towards small radii, and steeply dropping at the largest radii, leaving a “knee” where the profile has an approximately power law form. We examined each profile and determined the inner and outer radii at which the power-law portion begins and ends, respectively, and the fraction of the total H I mass  $\mathcal{M}_{\text{HI}}$  within those radii. On average 21( $\pm 10$ )% of  $\mathcal{M}_{\text{HI}}$  is interior to the inner radius and 75( $\pm 10$ )% is interior to the outer, hence the power law knee contains a bit over 50% of  $\mathcal{M}_{\text{HI}}$  on average. In order to treat the galaxies consistently, we determine the radii enclosing 25% and 75% of  $\mathcal{M}_{\text{HI}}$ ,  $R_1$  and  $R_2$  respectively, and fit a power law

$$\Sigma_g \propto R^N \quad (14)$$

to the points between these radii. The fits are shown in Fig. 2 with the parameters listed in the corners of the panels and

<sup>1</sup> The NASA/IPAC Extragalactic Database (NED) is operated by the Jet Propulsion Laboratory, California Institute of Technology, under contract with the National Aeronautics and Space Administration.

<sup>2</sup> full name: ESO215-G709 (Warren et al. 2004).

<sup>3</sup> full name: ADBSJ 113845+2008 (Cannon et al. 2009).

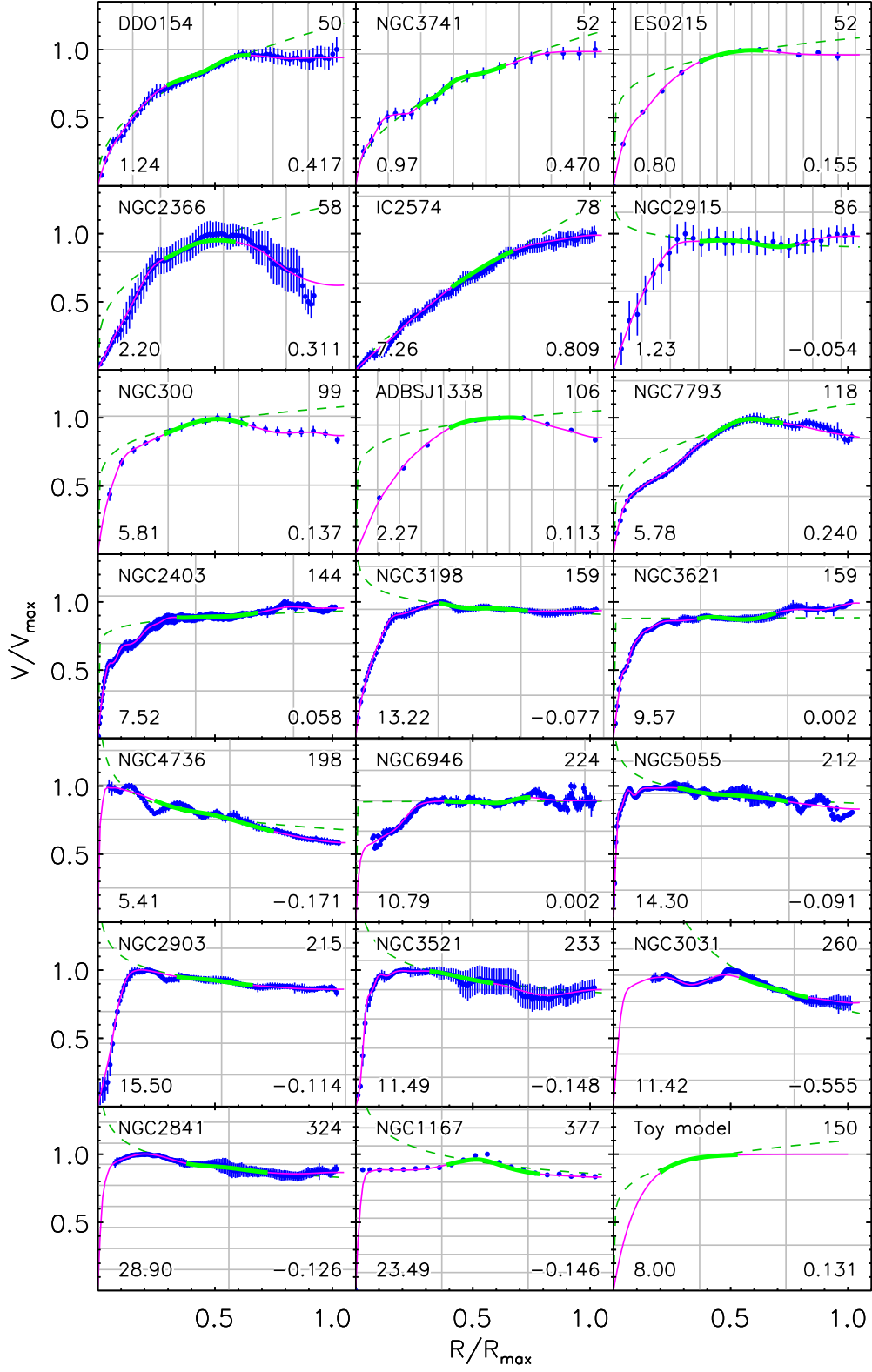


**Figure 1.** Rotation curves (RC), ordered and scaled by maximum rotational velocity,  $V_{\max}$ , plotted against radius  $R$  scaled by the maximum radius of the data  $R_{\max}$ . We show the measured points and their errors (blue), the adopted spline RC fits (magenta), with the middle 50% of the HI mass highlighted (green), and a power law fit to the data in this region (dashed green). Each panel lists the galaxy name is at upper left, the optical radius  $R_{25}$  in kpc at lower left,  $V_{\max}$  in  $\text{km s}^{-1}$  at upper right and the power law slope  $\gamma$  at lower right. Vertical (grey) lines mark intervals of  $R_{25}$ , while horizontal lines mark intervals of  $50 \text{ km s}^{-1}$ . The toy model plotted in the lower right panel is an RC of the form used by Leroy et al. (2008) with  $R_{\text{flat}} = 4 \text{ kpc}$ .

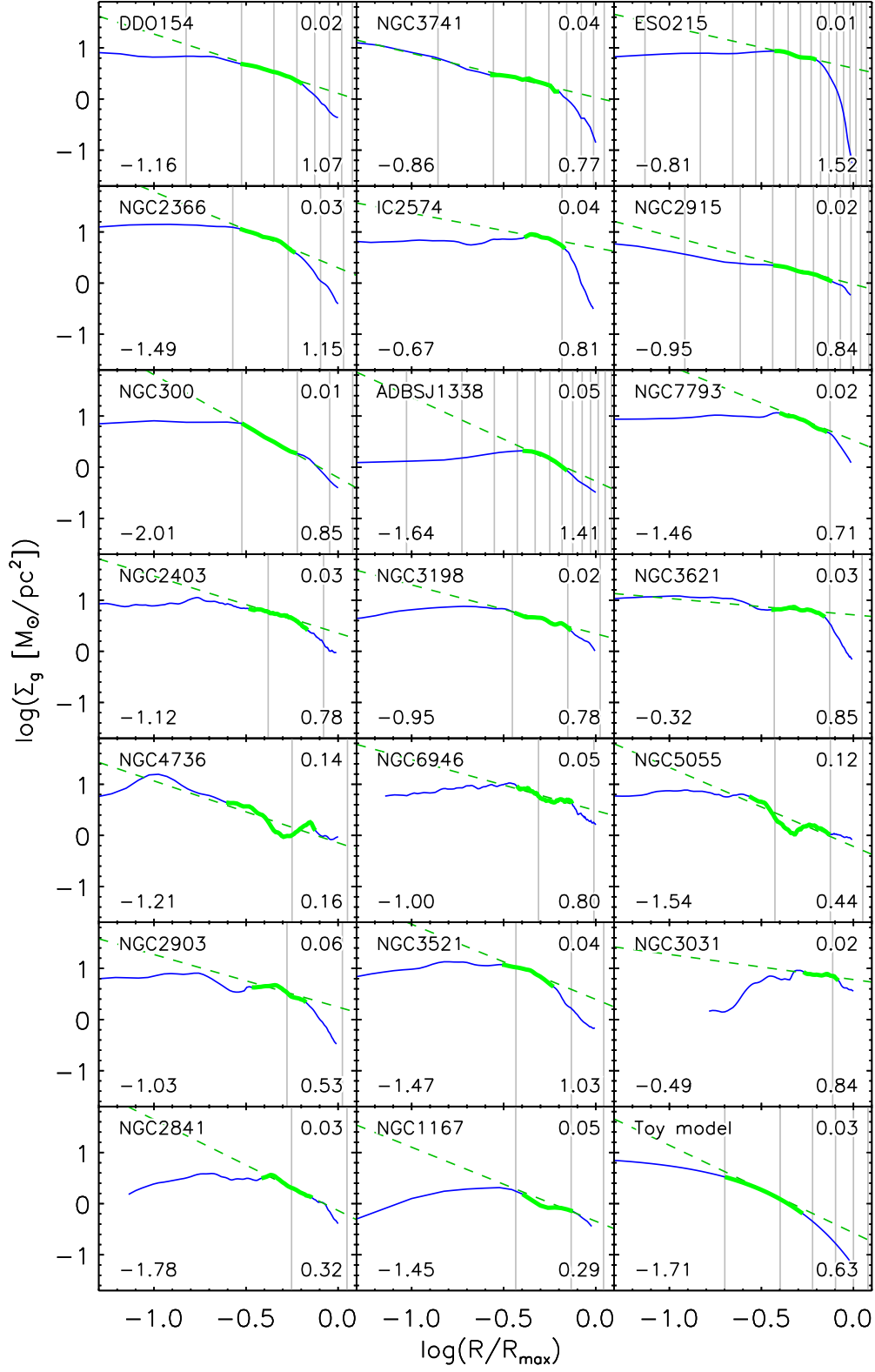


**Figure 2.** Radial profiles of ISM surface mass density  $\Sigma_g$  (blue) plotted on a log-log scale. Line colour and highlighting are the same as in Fig. 1. Power law fits to the highlighted portion of the profile are shown with dashed lines (dark green). Each panel lists dispersion of the residuals of the fits at upper right, the power law index  $N$  at lower left, and  $\log(\Sigma_g)$  at  $R_{25}$  at lower right. The toy model shown in the lower right panel is an exponential profile (eq. 15) with scale length  $\alpha^{-1} = R_{25}$  and central density  $\Sigma_{g,0} = 10 M_\odot \text{pc}^{-2}$ .

**Table 1.** Sample properties

Galaxy (1)	morphology (2)	$D$ (3)	$R_{25}$ (4)	$R_{\max}$ (5)	$\mathcal{M}_{\text{HI}}$ (6)	$V_{\max}$ (7)	Data ; distance source (8)
DDO154	IB(s)m	4.3	1.24	8.28	0.45	50	de Blok et al. (2008); Makarova et al. (1998)
NGC3741	Im	3.2	0.97	6.97	0.22	52	Gentile et al. (2007); Dalcanton et al. (2009)
ESO215	Im <sup>a</sup>	5.2	0.80	10.82	1.46	52	Warren et al. (2004); Karachentsev et al. (2007)
NGC2366	IB(s)m	3.4	2.20	8.20	0.81	58	Oh et al. (2008); Dalcanton et al. (2009)
IC2574	SAB(s)m	3.8	7.26	11.07	1.67	78	Oh et al. (2008); Dalcanton et al. (2009)
NGC2915	BCD <sup>b</sup>	4.1	1.23	10.12	0.49	86	Elson et al. (2010); Meurer et al. (2003)
NGC300	SA(s)d	2.0	5.81	19.36	2.55	99	Westmeier et al. (2011); Freedman et al. (2001)
ADBSJ1138	BCD <sup>c</sup>	50.0	2.27	24.20	1.92	106	Cannon et al. (2009); NED
NGC7793	SA(s)d	3.9	5.78	7.74	1.11	118	de Blok et al. (2008); Karachentsev et al. (2003b)
NGC2403	SAB(s)cd	3.2	7.52	18.01	3.59	144	de Blok et al. (2008); Freedman et al. (2001)
NGC3198	SB(rs)c	13.8	13.22	37.51	14.50	159	de Blok et al. (2008); Freedman et al. (2001)
NGC3621	SA(s)d	6.6	9.57	25.77	9.43	159	de Blok et al. (2008); Freedman et al. (2001)
NGC4736	(R)SA(r)ab	4.7	5.41	9.61	0.52	198	de Blok et al. (2008); Karachentsev et al. (2003a)
NGC6946	SAB(rs)cd	6.8	10.79	22.08	7.00	224	de Blok et al. (2008); Karachentsev et al. (2000)
NGC5055	SA(rs)bc	7.9	14.30	38.15	8.29	212	de Blok et al. (2008); Tully et al. (2009)
NGC2903	SA(rs)bc	8.9	15.50	29.34	6.45	215	de Blok et al. (2008); Drozdovsky & Karachentsev (2000)
NGC3521	SAB(rs)bc	10.7	11.49	31.17	12.70	233	de Blok et al. (2008)
NGC3031	SA(s)ab	3.6	11.42	14.80	4.05	260	de Blok et al. (2008); Freedman et al. (2001)
NGC2841	SA(r)b:	14.1	28.90	51.68	13.90	324	de Blok et al. (2008); Saha et al. (2006)
NGC1167	SA0 <sup>-</sup>	66.0	23.49	63.88	12.20	377	Struve et al. (2010); NED

Columns: (1) galaxy name; (2) galaxy morphology from the RC3 catalogue (de Vaucouleurs et al. 1991) except as following: a. Warren et al. (2004), b. Meurer et al. (1994), c. Cannon et al. (2009); (3) Distance in Mpc; (4) radius at the  $B$  band 25 mag arcsec<sup>-2</sup>; (5) radius of the outermost H I measurement; (6) H I mass in  $10^9 \mathcal{M}_{\odot}$ ; (7) Maximum rotation amplitude in km s<sup>-1</sup>.

in Table 2. The range  $R_1$  to  $R_2$  is highlighted in our figures by using thicker lines to plot the profiles.  $N$  spans the range  $-2.01$  (NGC 300) to  $-0.32$  (NGC 3621). The power law fit is reasonable. The average  $\epsilon_{\Sigma_g} = 0.042$  dex (10%), and in only two cases is  $\epsilon_{\Sigma_g} > 0.1$  dex (in NGC 4736, NGC 5055).

While we use a power law approximation of  $\Sigma_g$  for convenience, H I profiles are not always characterised as such in the literature. Ferguson & Clarke (2001), for example, use an exponential profile:

$$\Sigma_g = \Sigma_{g,0} e^{-\alpha R} \quad (15)$$

where  $\Sigma_{g,0}$  is the central ISM surface mass density and  $\alpha^{-1}$  is the disk scale length. They show that the ISM in their viscous disk models are well characterised by such a profile over a wide range in radii, with the ISM scale length greater than that of the stellar disk (which is well known to follow an exponential profile; Freeman 1970). The bottom right panel of Fig. 2 shows an exponential profile having  $\Sigma_{g,0} = 10 \mathcal{M}_{\odot} \text{pc}^{-2}$  and  $\alpha^{-1} = R_{25}$ . This profile is similar in shape to that of our sample. We fit a power law to this profile in the same manner as the sample galaxies, and report the results in Table 2 and Fig. 2. Over the relevant  $R_1$  to  $R_2$  a power law fit to an exponential profile gives a  $\epsilon_{\Sigma_g}$  of 0.03 dex (7%). In comparison, 55% of our sample have  $\epsilon_{\Sigma_g}$  less than or equal to this. Thus a power law is at least as good a functional form as an exponential for about half the sample.

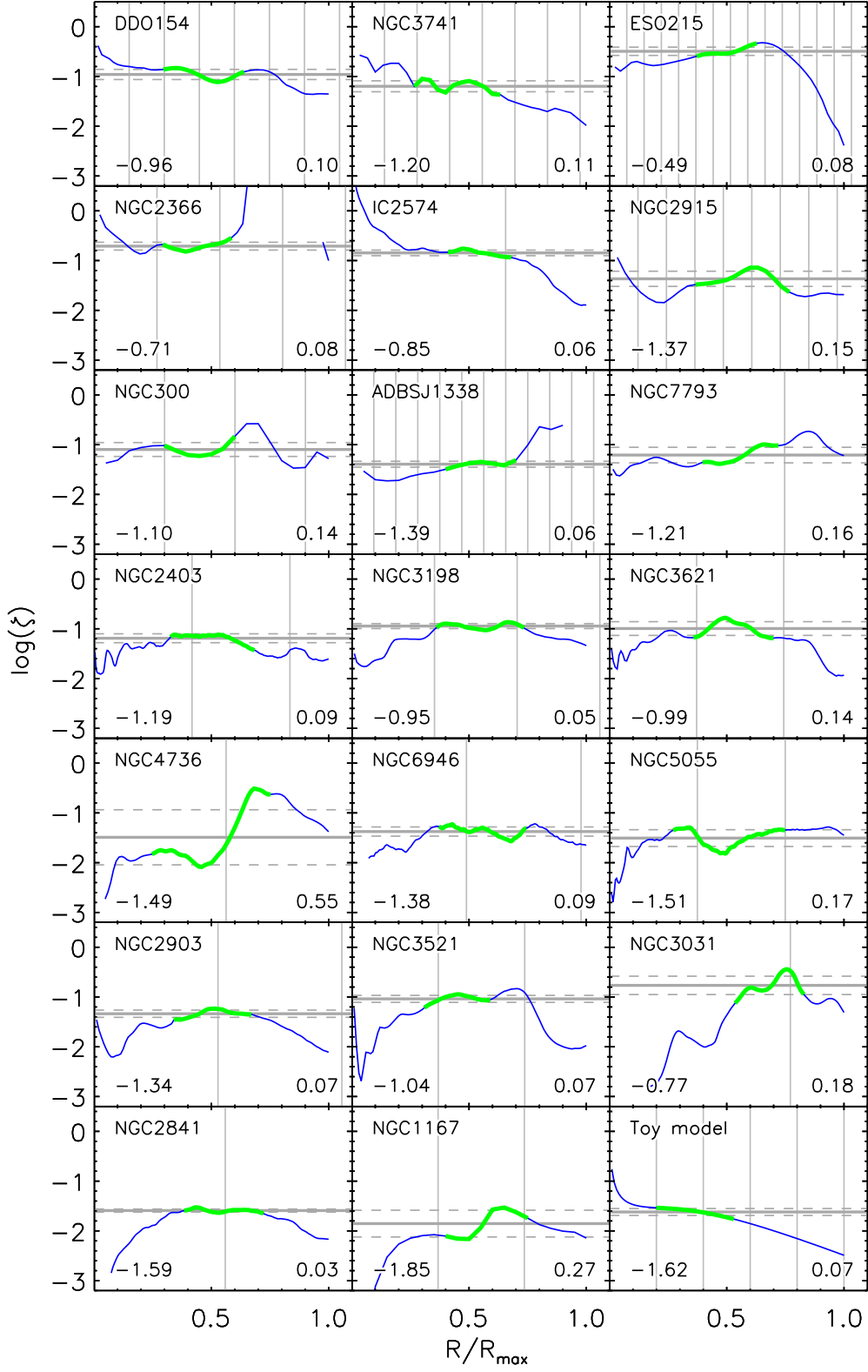
Figure 3 shows the  $\zeta$  profiles in order to test the premise that H I traces the total mass. To form the ratio we take  $\Sigma_g$  from the observed profile and  $\Sigma_M$  from eq. 5. In general the profiles are highly structured. This is due to irregularities in both the  $\Sigma_g$  and  $V$  profiles. The  $\zeta$  profiles are particularly sensitive to the latter since it depends on the derivative of the RC (eq. 5). The toy model, which combines the smooth RC shown in Fig. 1 and the smooth  $\Sigma_g$  profile shown in

Fig. 2, has  $\epsilon_{\zeta} = 0.07$  dex. Six of the galaxies in the sample have  $\zeta$  profiles that have  $\epsilon_{\zeta}$  at this level or smaller.

Figure 4 shows the  $Q$  profiles, for an assumed constant velocity dispersion  $\sigma = 8 \text{ km s}^{-1}$ . The average  $\log(Q)$  between  $R_1$  and  $R_2$  and the  $\epsilon$  in this value are listed in Table 2 and the panels of Fig. 4. For the majority of the sample  $Q$  is quite flat between  $R_1$  and  $R_2$ , and somewhat beyond for many cases. Over this range, the average  $\epsilon_Q$  is 0.06 dex (15%), while in two cases it is more than twice that: NGC 4736 and NGC 5055, for which the variation in  $Q$  corresponds largely to irregular structure in the  $\Sigma_g$  profile (Fig. 2). For NGC 2366,  $Q$  becomes undefined for much of the disk beyond  $R_2$  because, in this case, its RC is declining more steeply than a Keplerian decline. Since this is unphysical, it is likely that a warp or non-circular motions cause the RC of Oh et al. (2008) to be underestimated. In the bottom right panel we combine the toy models shown in Fig. 1 and Fig. 2. This model has  $\epsilon_Q = 0.09$  dex, while 70% of our sample have values less than or equal to this. As expected,  $Q$  is rising beyond  $R_2$  for the majority of the sample.

The  $\sigma = 8 \text{ km s}^{-1}$  we adopt is in the middle of the pack compared to what has been adopted in other studies; e.g. Kennicutt (1989) adopts  $\sigma = 6 \text{ km s}^{-1}$ , while Leroy et al. (2008) use  $\sigma = 11 \text{ km s}^{-1}$ . Changing to a different constant  $\sigma$  will only change  $Q$  by a constant multiplicative value. Following Tamburro et al. (2009) we also performed calculations where  $\sigma$  declined linearly with radius, using their profiles for the few overlapping cases between our study and theirs, and otherwise setting  $\sigma = 10 \text{ km s}^{-1}$  at  $R_{25}$  and falling linearly with radius to  $\sigma = 5 \text{ km s}^{-1}$  at the last measured point of the radial profiles. The resultant  $Q$  profile do not look very different from fig. 4; in particular, the decline in  $\sigma$  does not remove the rise in  $Q$  often found at large  $R$ .

While Fig. 4 shows that  $Q$  is fairly constant over radii



**Figure 3.** Profiles of the ratio  $\zeta$  of gas surface mass density  $\Sigma_g$  to projected total surface mass density  $\Sigma_M$ , plotted on a log scale, against linear scaled radius. Line colour and highlighting are the same as in Fig. 1. The average  $\log(\zeta)$  and dispersion about the average in the highlighted region is marked with the solid and dashed horizontal (gray) lines and listed at the lower left and lower right corners. The vertical lines show intervals of  $R_{25}$ .

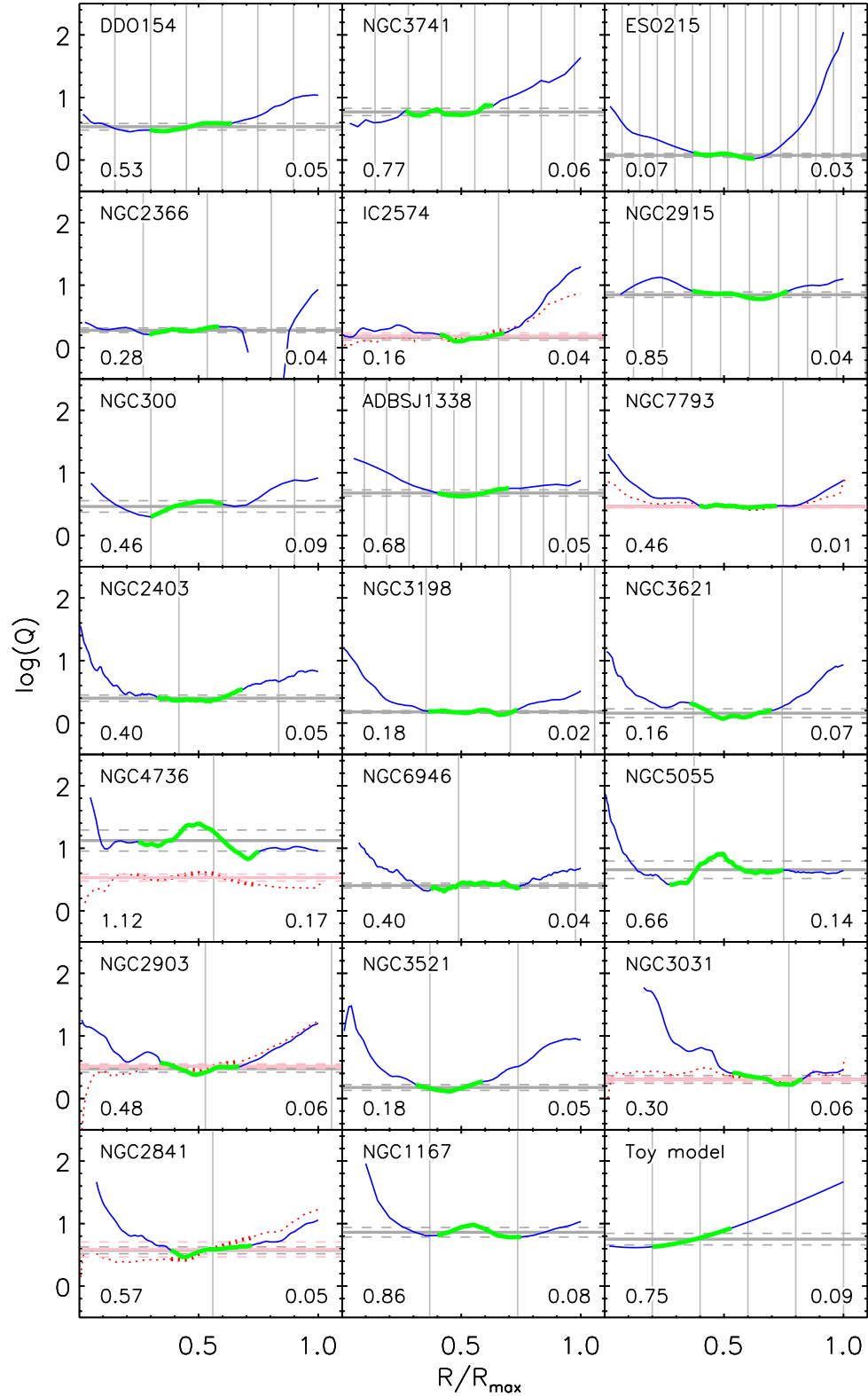


**Figure 4.** Toomre stability parameter  $Q$  profiles on a log scale, plotted against linear scaled radius. Line colour and highlighting are the same as in Fig. 1. The average  $\log(Q)$  in the highlighted region is marked at lower left and the rms about this average is given at lower right, and these are shown with the horizontal (grey) lines. The vertical lines show intervals of  $R_{25}$ . In the six cases where the fit range is largely within  $R_{25}$  we show profiles of the two fluid stability parameter  $Q_{2f}$  (Romeo & Wiegert 2011) as red dotted lines (thicker over the fit range); the pink thick line shows the average  $\log(Q_{2f})$  over the fit range and the pink dashed lines are offset from this by the rms about this average.



incorporating about half of the H I, usually it increases outside this range. The explanation of what is happening at large radii is fairly simple. There, RCs typically are flat or become flatter as can be seen in Fig 1. As shown by eq. 13, for  $\zeta$  to be constant in this limit requires  $\Sigma_g \propto R^{-1}$ . Such a profile can not be maintained to arbitrary radius because it would require infinite  $\mathcal{M}_{\text{HI}}$ . To have a disk with finite mass and angular momentum requires a more rapid drop-off in  $\Sigma_g$ , as is observed beyond  $R_2$  (Fig. 2), hence  $Q$  typically rises at the largest radii. Hoekstra et al. (2001) point out that the sharp drop off in  $\Sigma_g$  at large  $R$  does not correspond to an expected decline in RCs, thus casting doubt on the ability of H I to trace DM. Hessman & Ziebart (2011) counter that the fitting technique of Hoekstra et al. (2001) over emphasises the RC fits at large  $R$  where much of the hydrogen is ionised. Neutral or ionised, there is a finite ISM mass, and this will limit the ability of the ISM to trace DM.

There are multiple causes for the rising  $Q$  profiles towards small radii. The central parts of galaxies typically have a significant molecular content, which we have not included here, hence  $Q$  is overestimated. In addition, the stellar disk usually dominates the mass distribution, so that a single component  $Q$  is inadequate for determining the true disk stability (Leroy et al. 2008; Romeo & Wiegert 2011). Our assumption has been that the H I largely resides in the outer disk. However, in six of the sample galaxies (IC 2574, NGC 7793, 4736, 2903, 3031, and 2841) the fitting range is largely interior to  $R_{25}$ , hence the stellar disk is likely to play an important role in determining the stability of the disk in these cases.

In order to determine the true disk stability for these cases, we calculated the two fluid (stars and gas) stability parameter  $Q_{2f}$ . There are various formulations of the two fluid stability parameter (e.g. Jog & Solomon 1984; Wang & Silk 1994; Rafikov 2001; Romeo & Wiegert 2011). Here, we calculate  $Q_{2f}$  from eq. 9 of Romeo & Wiegert (2011) which accounts for the thickness of the stellar and gaseous disks. It can be rewritten in a simplified form as

$$\frac{1}{Q_{2f}} = \frac{p_\star}{Q_\star} + \frac{p_g}{Q_g} \quad (16)$$

Where  $Q_\star$  and  $Q_g$  are the stability parameters for the stellar and gaseous components of the disk calculated separately using eq. 1, and  $p_\star$ ,  $p_g$  are weight factors which depend on the velocity dispersions of the stars and gas and the value of  $Q_\star$  compared to  $Q_g$ . Calculation of  $Q_{2f}$  requires the stellar mass density  $\Sigma_\star$  in the disk which we derive from the stellar mass radial profiles of de Blok et al. (2008), and the radial component of the stellar velocity dispersion ellipsoid  $\sigma_{\star,r}$ . We take  $\sigma_{\star,r} \approx \sigma_{\star,z}/0.6$  following Shapiro et al. (2003) where  $\sigma_{\star,z}$  is the vertical component of the stellar velocity dispersion. This is given by

$$\sigma_{\star,z} = \sqrt{2\pi G \Sigma_{\text{disk}} h_\star} \quad (17)$$

where  $\Sigma_{\text{disk}} = \Sigma_\star + \Sigma_g$  is the total disk surface mass density and  $h_\star$  is the stellar disk scale height. Following Leroy et al. (2008) we estimate the scale height from the disk scale length using  $h_\star \sim l_\star/7.3$  and fit the exponential scale length  $l_\star$  over the same fit region as highlighted in our figures. While we are primarily concerned with  $Q_{2f}$  over the fitted region it is instructive to also see its behaviour beyond this range. In the central regions, in cases where the measured  $\Sigma_\star$  is greater

than the extrapolated exponential fit, we replace  $\Sigma_\star$  with this fit, under the assumption that the excess light represents a bulge or thick disk with a scale height larger than the disk and thus has a lesser contribution to the disk potential than is expected for the surface brightness. Similarly, at large  $R$ , beyond the last measured  $\Sigma_\star$ , we also adopt the extrapolated fit when calculating  $Q_{2f}$ . The results of the  $Q_{2f}$  calculations are shown in Fig 4 as the red dotted lines. The average  $\log(Q_{2f})$  over the fitted range is shown as the thick pink lines and the dashed pink lines are offset from this line by its rms.

Figure 4 demonstrates that the  $Q_{2f}$  profiles are flatter than the  $Q = Q_g$  profiles when the entire radial range is considered. The biggest difference is for NGC 4736 where the average  $\pm$  dispersion is  $\langle \log(Q_{2f}) \rangle = 0.53 \pm 0.06$  over the fitted region; the dispersion is a factor of three lower than that for the gas  $Q$ . For the remaining cases, the difference between  $Q$  and  $Q_{2f}$  are more subtle, over the fitted range where we find  $\langle \log(Q_{2f}) \rangle = 0.17 \pm 0.05$ ,  $0.46 \pm 0.02$ ,  $0.052 \pm 0.04$ ,  $0.30 \pm 0.04$ , and  $0.59 \pm 0.12$  for IC 2574, NGC 7793, 2903, 3031, and 2841 respectively. The dispersion in  $\log(Q_{2f})$  is smaller than that of  $\log(Q)$  for half the cases: NGC 4736, 2903, and 3031. In most cases  $Q$  is an adequate proxy for the total disk stability parameter  $Q_{2f}$  at the radii we are interested in here, even when much of the H I is within the optical radius. However, a more sophisticated analysis, such as using  $Q_{2f}$  is required to extend the analysis even closer to the center, or in cases like NGC 4736 where the stellar disk strongly dominates the gaseous disk at all radii. In Zheng et al. (2012) we perform such an analysis over the optically bright portion of galaxies, using various prescriptions for  $Q_{2f}$ . There we show that the assumption of a constant stability disk can explain the relative distributions of gas, stars and star formation over much of the optically bright portion of galaxies.

Close examination of Fig. 1 and Fig. 2 shows that another of our premises is not exactly correct: the RCs are not always flat. Instead there is a rather wide distribution of rotation curve power law indices  $\gamma$ . What then causes the nearly constant  $Q$  seen in Fig. 4? This requires the numerator and denominator in the defining equation (eq. 1) to have the same shape, i.e. the same slope. For a constant  $\sigma$ , this requires the  $\kappa$  and  $\Sigma_g$  profiles to have the same shape. To test this, we fit a power law  $\kappa \propto R^M$  to the epicyclic frequency profile. The  $\kappa$  profiles and the fits to them are shown in Fig. 5, with the relevant fit parameters listed in Table 2 and the panels of Fig. 5. A power law form is a reasonable approximation to the  $\kappa$  profiles between  $R_1$  and  $R_2$ .

Figure 6 plots the power law index in  $\Sigma_g$ ,  $N$  against the power law index in  $\kappa$ ,  $M$ . There is a crude correlation between the indices; the Pearson's correlation coefficient  $r_{xy} = 0.45$ , with a 2% chance that the correlation is random. Examination of the figure shows that there are two obvious outliers, and we can see plausible reasons for their discrepant behaviour in each case. NGC 3031 (M81) is in a nearby highly interactive group with three close companions (M82, NGC 3077, and HoIX). These may affect the outer ISM distribution of NGC 3031 through either stripping material, or having material stripped from them. NGC 300 has a very extended and lopsided H I distribution and the steepest  $N = -2.01$  in our sample. Westmeier et al. (2011) note that there are morphological signs of ram-pressure stripping

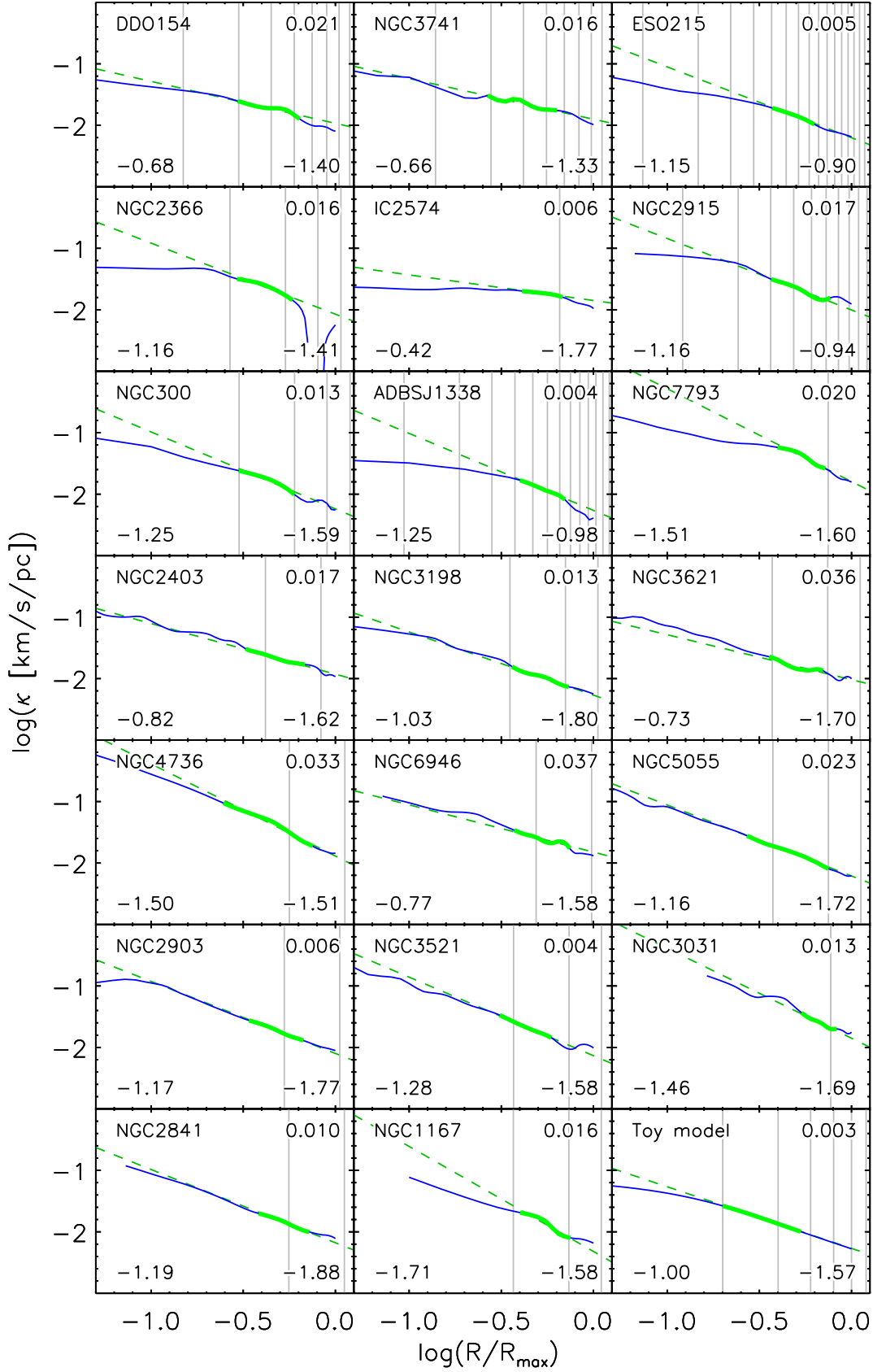


**Figure 5.** Epicyclic frequency  $\kappa$  profiles on a log-log scale. Line colour and highlighting are the same as in Fig. 1. In each panel, the rms of the power-law fits (green dashed lines) are listed at upper right, the power law index  $M$  at lower left, and  $\log(\kappa)$  at  $R_{25}$  at lower right.

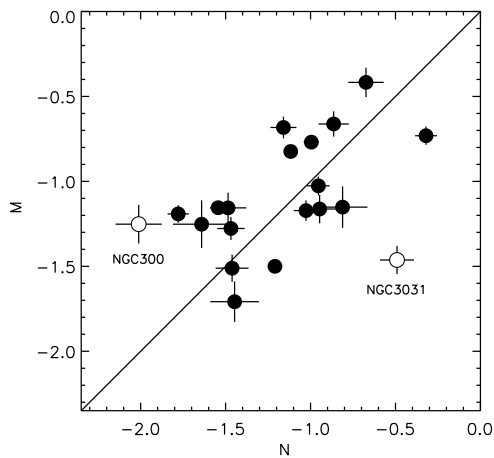


**Figure 6.** Index  $N$  of the fit to the  $\Sigma_g$  profiles in Fig. 2 plotted against the index  $M$  of the fit to the  $\kappa$  profiles shown in Fig. 5. The diagonal line marks  $N = M$ . Outliers are plotted as hollow circles, are labelled, and discussed further in the text.

of the outer disk, which could steepen the  $\Sigma_g$  profile. They also note that their ATCA data may not capture the total H I flux due to missing short spacings. The  $\Sigma_g$  profile we use was derived from a data cube that combined the ATCA data of Westmeier et al. (2011) and single dish H I data from the Parkes 64m telescope obtained for the GASS project (Kalberla et al. 2010), thus recovering the H I flux missing from the ATCA observations<sup>4</sup>. Excluding these two galaxies  $r_{xy} = 0.63$ , with a 0.3% chance of being random. We conclude that there is modest correlation between the indices which scatter about the line  $N = M$ , that is the  $\kappa$  and  $\Sigma_g$  profiles have the same shape. This is exactly what is needed for a constant  $Q$  disk.

A further test of the hypothesis that galaxy disks evolve to constant  $Q$  is given by eq. 12 which predicts that  $\zeta$  and  $V_{\max}$  should be anti-correlated. These quantities are plotted (in the log) in Fig. 7. The filled circles show the average  $\log(\zeta)$  (i.e.  $\langle \log(\zeta) \rangle$ ), between  $R_1$  and  $R_2$  as marked in fig. 3. The expected anti-correlation is clearly present, with  $r_{xy} = -0.60$ ; the probability that this is due to random sampling of uncorrelated data is less than 0.3%. The solid line shows the expected anti-correlation for galaxies with a flat RC, eq. 12, and for the assumed  $\sigma = 8 \text{ km s}^{-1}$  and  $Q = 3$  (this corresponds to the average  $\log(Q)$  for our sample). The dashed line is a  $\chi^2$  fit to the data:

$$\langle \log(\zeta) \rangle = (0.83 \pm 0.13) - (0.93 \pm 0.06) \log(V_{\max}). \quad (18)$$

The dispersion about this fit  $\epsilon_{\log(\zeta)} = 0.28$  dex, while the average offset between the expected relation and this fit is 0.08 dex, very close to what is expected from the standard error on the mean, 0.06 dex. This demonstrates that eq. 12 provides a reasonable model for the average gas to total mass ratio between  $R_1$  and  $R_2$ .

The hollow circles in Fig. 7 show the ratio  $\mathcal{Z}$  plotted

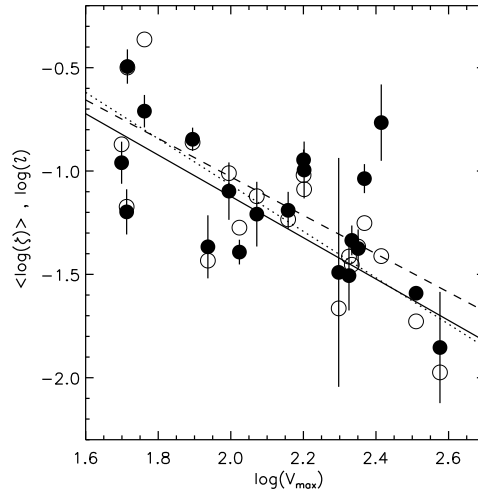


**Figure 7.** Average  $\log(\zeta)$  between  $R_1$  and  $R_2$ ,  $\langle \log(\zeta) \rangle$ , plotted as filled circles against rotation curve maximum  $V_{\max}$ . The error bars represent  $\epsilon_{\zeta}$ . The hollow circles represent the integrated ratio  $\mathcal{Z}$  for the same galaxies. The solid line shows the expected relationship for galaxies with a flat RC, eq. 12, and  $\sigma = 8 \text{ km s}^{-1}$ ,  $Q = 3$ . The dashed line shows the fit to the  $\langle \log(\zeta) \rangle$  data reported in eq. 18, while the dotted line shows the fit to the  $\mathcal{Z}$  data reported in eq. 19.

against  $V_{\max}$ . These quantities are even more strongly anti-correlated with  $r_{xy} = -0.80$  and a less than 0.002% chance that the correlation is due to random sampling of uncorrelated data. The dotted line shows an equally weighted least squares fit to the data

$$\log(\mathcal{Z}) = (1.17 \pm 0.19) - (1.12 \pm 0.09) \log(V_{\max}); \quad (19)$$

the dispersion about this fit  $\epsilon_{\log(\zeta)} = 0.24$  dex. This is tighter than eq. 18, probably because  $\mathcal{Z}$  is better defined than  $\langle \log(\zeta) \rangle$  which is more susceptible to noise in the  $\Sigma_g$  and  $V$  profiles.

## 4 DISCUSSION AND CONCLUSIONS

The correlation between the shape of the  $\kappa$  and  $\Sigma_g$  profiles shown in Fig. 6 is profound. Since  $M$  is determined purely by the potential, this implies that the ISM disk is responding to the potential, and hence that secular evolution is driving the correlation. An alternate hypothesis is that the structure of galactic disks is set by the mass and angular momentum accretion history (Barnes 2002; Sancisi et al. 2008). However, it is not clear why there should be any such correlation under this scenario. CDM simulations indicate that Milky-Way mass galaxies have had typically only two major merger event since  $z \sim 2$  (D’onghia et al. 2008; Cole et al. 2007), 10 Gyr ago, which agrees with observations of mergers (Conselice et al. 2008). So, to the extent the accretion is from major-mergers, the outer disks should be very lumpy. Our sample does include some lumpy disks (e.g. NGC 4736 and NGC 5055) and also some galaxies that may currently be interacting (NGC 300, NGC 3031) perhaps contributing to the scatter and outliers in Fig. 6. The fact that the majority of the sample falls on the  $N = M$  line suggests that most

<sup>4</sup> Without the Parkes data we would have an even steeper  $N = -2.36$ .

are not strongly interacting and that prior interactions happened far enough in the past that the disk has re-stabilised and smoothed out to trace  $\kappa$ . The timescale for doing this is the orbital time  $t_{\text{orb}}$  ( $\sim 3t_{\text{dyn}}$  where  $t_{\text{dyn}}$  is the dynamical timescale). For our sample, the average  $t_{\text{orb}}(R_2) = 0.6$  Gyr. Taking the separation between major merger events to be 3 Gyr, there should be approximately five orbits between mergers, sufficient time for structure in the disk to smooth out. Alternatively, if accretion is slow “cold accretion” (Kereš et al. 2005; Sancisi et al. 2008) the disk would not be expected to be lumpy. However, that scenario does not provide an obvious explanation for the  $\Sigma_g$  and  $\kappa$  profiles following each other. Of course, cold accretion combined with feedback to equalize  $Q$ , as advocated here, is consistent with our results.

Previous studies have noted the large scatter in the HI to total or DM ratio (e.g. Bosma 1981; Hoekstra et al. 2001). This is hard to explain in the context of H I being a linear tracer of a baryonic DM (Hoekstra et al. 2001). We show that an inverse correlation between  $\zeta$  and  $V_{\text{max}}$  is expected from constant  $Q$  disks (eq. 12), and indeed is observed (Fig. 7). This avoids the need to place implausibly large quantities of molecular gas in disks. By linking a luminous component of the disk to the rotational velocity the  $\mathcal{Z} - V_{\text{max}}$  relation is reminiscent of the Tully-Fisher relation (Tully & Fisher 1977) and the baryonic Tully-Fisher relation (Freeman 1999; McGaugh et al. 2000). However, since  $\mathcal{Z}$  is a ratio, it does not provide a means to estimate ISM mass from  $V_{\text{max}}$ . To do so, one needs to know the extent of the H I mass distribution, since in the case of  $\gamma = 0$  the local  $\zeta$  and the integrated gas to total mass ratio within  $R$  remain constant and equal to each other. Alternatively, if one has  $\mathcal{M}_{\text{HI}}$  and  $V_{\text{max}}$  one can estimate the extent of the ISM distribution. This is typically the case in blind H I surveys, such as HIPASS (Barnes et al. 2001), and ALFALFA (Giovannelli et al. 2005) where the H I flux is known but the source is unresolved. Then one can use eq. 19 to estimate  $\mathcal{Z}$  and from that the maximum H I extent

$$R_{\text{max}} = \frac{G\mathcal{M}_{\text{HI}}}{\mathcal{Z}V_{\text{max}}^2}. \quad (20)$$

This may be useful for determining whether follow-up observations of a particular galaxy are likely to be fruitful, or estimating the covering factor of H I absorbers (e.g. Zwaan et al. 2005).

Our results imply that secular processes are important for setting disk structure. Lynden-Bell & Pringle (1974) noted that viscous disks should evolve so that mass is concentrated in the centre and angular-momentum goes to infinity. As dissipative encounters cause ISM mass to be funnelled towards the galaxy centre, the disk must also spread to conserve angular momentum, and the ISM disk size should grow with time (e.g. Ferguson & Clarke 2001). High resolution simulations of galactic disks show that transient density waves can increase the size of disks and alter their metallicity distributions (Roškar et al. 2008a,b). The flattening of metallicity gradients (Werk et al. 2010, 2011) in outer disks may be evidence of ISM circulation in spreading disks. If disks are spreading now, they should have been denser and more compact in the past. This would imply a higher molecular fraction from the increased hydrostatic pressure, as well as increased total gas content (to account

for the stars that have since formed). Braun et al. (2011) noted an order of magnitude increase in the molecular mass for the most luminous star forming galaxies from now to  $z \sim 0.4$ , mirroring the increase in the cosmic star formation rate density  $\rho_{\text{SFR}}(z)$  (e.g. Hopkins & Beacom 2006). They argue that this implies that recent star formation evolution is largely due to the run down in the available ISM supply. Hanish et al. (2006) made a similar argument based on the slope in  $\rho_{\text{SFR}}(z)$  being similar to that expected from the star formation law. As outer disks spread and evolve,  $Q$  should remain constant with radius. The exact values of  $Q$  and  $\sigma$  will be set by feedback (with less efficient star formation in the thinning disk) and the available angular momentum.

Finally, our results do not disprove MOND, nor do they rule out the possibility that some or most of the DM is in a gaseous form. However, some of the appeal of these theories is that it was not clear under the prevailing CDM paradigm why dissipative gaseous disks should trace the non-dissipative CDM halo which resides in a spheroid. Our work provides this linkage by showing that ISM disks will trace DM as a natural consequence of disk stabilisation, and our tests of the H I dominated outer disks are consistent with that interpretation.

## ACKNOWLEDGMENTS

GRM thanks Claude Carignan for first pointing out the relationship between DM and H I to him in 1992. We thank John Cannon, Ed Elson, Gianfranco Gentile, Christian Struve, Brad Warren, and Tobias Westmeier for providing us with data from their studies. We are especially grateful to Tobias Westmeier for combining his ATCA data of NGC 300 with archival Parkes observations and extracting a new radial profile for us. We thank Ken Freeman and Alan Duffy for useful comments, and the referee Alessandro Romeo for making suggestions that improved the paper. GRM was supported in part by a Research Collaboration Award from the University of Western Australia. ZZ was supported through Galex GI grant NNX09AF85G. This research has made use of the NASA/IPAC Extragalactic Database (NED) which is operated by the Jet Propulsion Laboratory, California Institute of Technology, under contract with the National Aeronautics and Space Administration.

**Note added in proof:** We note a previous paper that reached similar conclusions that had escaped our attention. Struck-Marcell (1991, ApJ, 368, 348) used a related approach, the assumption that gas disks maintain a balance of hydrostatic forces, to derive a disk structure of  $\Sigma_g \propto R^{-1}$  for disks having a flat RC. That paper briefly alludes to the relationship with DM, but does not generalize the problem to arbitrary RC shape as we have done.

## REFERENCES

- Barnes D. G., Staveley-Smith L., de Blok W. J. G., et al., 2001, MNRAS, 322, 486
- Barnes J. E., 2002, MNRAS, 333, 481
- Bosma A., 1981, AJ, 86, 1825

- Bournaud F., Duc P.-A., Brinks E., et al., 2007, *Science*, 316, 1166
- Braun R., Popping A., Brooks K., et al., 2011, *MNRAS*, 416, 2600
- Broeils A. H., 1992, *A&A*, 256, 19
- Cannon J. M., Salzer J. J., Rosenberg J. L., 2009, *ApJ*, 696, 2104
- Carignan C., Beaulieu S., 1989, *ApJ*, 347, 760
- Carignan C., Charbonneau P., Boulanger F., et al., 1990, *A&A*, 234, 43
- Carignan C., Puche D., 1990a, *AJ*, 100, 394
- Carignan C., Puche D., 1990b, *AJ*, 100, 641
- Cole S., Helly J., Frenk C. S., et al., 2007, *MNRAS*, 383, 546
- Conselice C. J., Rajgor S., Myers R., 2008, *MNRAS*, 386, 909
- Dalcanton J. J., Williams B. F., Seth A. C., et al., 2009, *ApJS*, 183, 67
- de Blok W. J. G., Walter F., Brinks E., et al., 2008, *AJ*, 136, 2648
- de Vaucouleurs G., de Vaucouleurs A., Corwin H. G., et al., 1991, *Third Reference Catalogue of Bright Galaxies*. Springer Verlag
- Debattista V., Mayer L., Carollo C., et al., 2006, *ApJ*, 645, 209
- D'onghia E., Mapelli M., Moore B., 2008, *MNRAS*, 389, 1275
- Drozdovsky I. O., Karachentsev I. D., 2000, *A&AS*, 142, 425
- Elson E. C., de Blok W. J. G., Kraan-Korteweg R. C., 2010, *MNRAS*, 404, 2061
- Faber S. M., Gallagher J., 1979, *ARA&A*, 17, 135
- Ferguson A., Wyse R., Gallagher J., et al., 1998, *ApJ*, 506, L19
- Ferguson A. M. N., Clarke C. J., 2001, *MNRAS*, 325, 781
- Freedman W. L., Madore B. F., Gibson B. K., et al., 2001, *ApJ*, 553, 47
- Freeman K. C., 1970, *ApJ*, 160, 811
- Freeman K. C., 1999, in Davies J. I., Impey C., Phillipps S., eds, "The Low Surface Brightness Universe", IAU Col 171, ASP Conf Series, #170 . p. 3
- Gentile G., Salucci P., Klein U., et al., 2007, *MNRAS*, 375, 199
- Gerhard O., Silk J., 1996, *ApJ*, 472, 34
- Giovanelli R., Haynes M. P., Kent B. R., et al., 2005, *AJ*, 130, 2598
- Hanish D. J., Meurer G. R., Ferguson H. C., et al., 2006, *ApJ*, 649, 150
- Hessman F. V., Ziebart M., 2011, *A&A*, 532, 121
- Hoekstra H., van Albada T. S., Sancisi R., 2001, *MNRAS*, 323, 453
- Hohl F., 1971, *ApJ*, 168, 343
- Hopkins A. M., Beacom J. F., 2006, *ApJ*, 651, 142
- Jobin M., Carignan C., 1990, *AJ*, 100, 648
- Jog C. J., Solomon P. M., 1984, *ApJ*, 276, 114
- Kalberla P. M. W., McClure-Griffiths N. M., Pisano D. J., et al., 2010, *A&A*, 521, 17
- Karachentsev I. D., Grebel E. K., Sharina M. E., et al., 2003b, *A&A*, 404, 93
- Karachentsev I. D., Sharina M. E., Dolphin A. E., et al., 2003a, *A&A*, 398, 467
- Karachentsev I. D., Sharina M. E., Huchtmeier W. K., 2000, *A&A*, 362, 544
- Karachentsev I. D., Tully R. B., Dolphin A., et al., 2007, *AJ*, 133, 504
- Kennicutt R. C., 1989, *ApJ*, 344, 685
- Kent S. M., 1987, *AJ*, 93, 816
- Kereš D., Katz N., Weinberg D. H., et al., 2005, *MNRAS*, 363, 2
- Leroy A. K., Walter F., Brinks E., et al., 2008, *AJ*, 136, 2782
- Lynden-Bell D., Pringle J. E., 1974, *MNRAS*, 168, 603
- McGaugh S. S., Schombert J. M., Bothun G. D., et al., 2000, *ApJ*, 533, L99
- Makarova L., Karachentsev I., Takalo L. O., et al., 1998, *A&AS*, 128, 459
- Markwardt C. B., 2009, *Astronomical Data Analysis Software and Systems XVIII ASP Conference Series*, 411, 251
- Mestel L., 1963, *MNRAS*, 126, 553
- Meurer G. R., Blakeslee J. P., Sirianni M., et al., 2003, *ApJ*, 599, L83
- Meurer G. R., Carignan C., Beaulieu S. F., et al., 1996, *AJ*, 111, 1551
- Meurer G. R., Mackie G., Carignan C., 1994, *AJ*, 107, 2021
- Mould J. R., Huchra J. P., Freedman W. L., et al., 2000, *ApJ*, 529, 786
- Oh S.-H., de Blok W. J. G., Walter F., et al., 2008, *AJ*, 136, 2761
- Olling R. P., Merrifield M. R., 2000, *MNRAS*, 311, 361
- Pfenniger D., Combes F., 1994, *A&A*, 285, 94
- Pfenniger D., Combes F., Martinet L., 1994, *A&A*, 285, 79
- Pfenniger D., Revaz Y., 2005, *A&A*, 431, 511
- Rafikov R. R., 2001, *MNRAS*, 323, 445
- Romeo A. B., Wiegert J., 2011, *MNRAS*, 416, 1191
- Roškar R., Debattista V. P., Quinn T. R., et al., 2008b, *ApJ*, 684, L79
- Roškar R., Debattista V. P., Stinson G. S., et al., 2008a, *ApJ*, 675, L65
- Rubin V. C., Thonnard N., Ford W. K. J., 1978, *ApJ*, 225, L107
- Safronov V. S., 1960, *Annales d'Astrophysique*, 23, 979
- Saha A., Thim F., Tammann G. A., et al., 2006, *ApJS*, 165, 108
- Sancisi R., 1983, in "Internal kinematics and dynamics of galaxies" *Proceedings of the IAU Symposium*, 100, 55
- Sancisi R., Fraternali F., Oosterloo T., et al., 2008, *A&AR*, 15, 189
- Sanders R. H., McGaugh S. S., 2002, *ARA&A*, 40, 263
- Sellwood J. A., Carlberg R. G., 1984, *ApJ*, 282, 61
- Shapiro K., Gerssen J., van der Marel R. P., 2003, *AJ*, 126, 2707
- Struve C., Oosterloo T., Sancisi R., et al., 2010, *A&A*, 523, 75
- Tamburro D., Rix H.-W., Leroy A. K., et al., 2009, *AJ*, 137, 4424
- Thilker D. A., Bianchi L., Boissier S., et al., 2005, *ApJ*, 619, L79
- Thilker D. A., Bianchi L., Meurer G., et al., 2007, *ApJS*, 173, 538
- Toomre A., 1964, *ApJ*, 139, 1217
- Tully R. B., Fisher J. R., 1977, *A&A*, 54, 661
- Tully R. B., Rizzi L., Shaya E. J., et al., 2009, *AJ*, 138, 323
- van der Hulst J. M., Skillman E. D., Smith T. R., et al., 1993, *AJ*, 106, 548

- Wada K., Meurer G., Norman C. A., 2002, ApJ, 577, 197  
Wang B., Silk J., 1994, ApJ, 427, 759  
Warren B. E., Jerjen H., Koribalski B. S., 2004, AJ, 128, 1152  
Werk J. K., Putman M. E., Meurer G. R., et al., 2010, ApJ, 715, 656  
Werk J. K., Putman M. E., Meurer G. R., et al., 2011, ApJ, 735, 71  
Westmeier T., Braun R., Koribalski B. S., 2011, MNRAS, 410, 2217  
Zheng Z., Meurer G. R., Heckman T. M., et al., 2012, MNRAS, (submitted)  
Zwaan M. A., van der Hulst J. M., Briggs F. H., et al., 2005, MNRAS, 364, 1467

**Table 2.** Fitted quantities

Galaxy (1)	$R_1$ (2)	$R_2$ (3)	zpt (4)	RC fit			$\Sigma_g$ fit			$\kappa$ fit			$\log(\zeta)$		$\log(Q)$	
				$\gamma$ (5)	$\epsilon$ (6)	zpt (7)	$N$ (8)	$\epsilon$ (9)	zpt (10)	$M$ (11)	$\epsilon$ (12)		avg (13)	$\epsilon$ (14)	avg (15)	$\epsilon$ (16)
DDO154	2.4	5.4	1.42	0.417(0.036)	0.005	1.07	-1.16(0.08)	0.02	-1.40	-0.68(0.06)	0.021		-0.96	0.10	0.53	0.05
NGC3741	1.8	4.5	1.36	0.470(0.077)	0.012	0.77	-0.86(0.09)	0.04	-1.33	-0.66(0.07)	0.016		-1.20	0.11	0.77	0.06
ESO215	3.9	7.0	1.57	0.155(0.005)	0.006	1.52	-0.81(0.15)	0.01	-0.90	-1.15(0.12)	0.005		-0.49	0.08	0.07	0.03
NGC2366	2.3	4.9	1.67	0.311(0.086)	0.010	1.15	-1.49(0.11)	0.03	-1.41	-1.16(0.09)	0.016		-0.71	0.08	0.28	0.04
IC2574	4.5	7.5	1.82	0.809(0.091)	0.008	0.81	-0.67(0.10)	0.04	-1.77	-0.42(0.09)	0.006		-0.85	0.06	0.16	0.04
NGC2915	3.6	7.9	1.94	-0.054(0.109)	0.008	0.84	-0.95(0.10)	0.02	-0.94	-1.16(0.08)	0.017		-1.37	0.15	0.85	0.04
NGC300	5.3	12.5	1.96	0.137(0.057)	0.011	0.85	-2.01(0.14)	0.01	-1.59	-1.25(0.11)	0.013		-1.10	0.14	0.46	0.09
ADBSJ1338	9.5	17.5	1.93	0.113(0.017)	0.007	1.41	-1.64(0.17)	0.05	-0.98	-1.25(0.14)	0.004		-1.39	0.06	0.68	0.05
NGC7793	3.1	5.7	2.08	0.240(0.042)	0.013	0.71	-1.46(0.10)	0.02	-1.60	-1.51(0.08)	0.020		-1.21	0.16	0.46	0.01
NGC2403	5.9	12.4	2.10	0.058(0.015)	0.004	0.78	-1.12(0.04)	0.03	-1.62	-0.82(0.03)	0.017		-1.19	0.09	0.40	0.05
NGC3198	13.2	27.8	2.20	-0.077(0.018)	0.005	0.78	-0.95(0.07)	0.02	-1.80	-1.03(0.06)	0.013		-0.95	0.05	0.18	0.02
NGC3621	9.1	18.0	2.15	0.002(0.013)	0.004	0.85	-0.32(0.06)	0.03	-1.70	-0.73(0.05)	0.036		-0.99	0.14	0.16	0.07
NGC4756	2.3	7.3	2.18	-0.171(0.015)	0.018	0.16	-1.21(0.04)	0.14	-1.51	-1.50(0.03)	0.033		-1.49	0.55	1.12	0.17
NGC6946	8.1	16.5	2.30	0.002(0.007)	0.009	0.80	-1.00(0.05)	0.05	-1.58	-0.77(0.04)	0.037		-1.38	0.09	0.40	0.04
NGC5055	10.3	28.6	2.31	-0.091(0.013)	0.008	0.44	-1.54(0.03)	0.12	-1.72	-1.16(0.02)	0.023		-1.51	0.17	0.66	0.14
NGC2903	9.8	19.7	2.30	-0.114(0.021)	0.004	0.53	-1.03(0.07)	0.06	-1.77	-1.17(0.06)	0.006		-1.34	0.07	0.48	0.06
NGC3521	9.6	18.5	2.36	-0.148(0.063)	0.009	1.03	-1.47(0.08)	0.04	-1.58	-1.28(0.07)	0.004		-1.04	0.07	0.18	0.05
NGC3031	7.8	12.3	2.32	-0.555(0.031)	0.002	0.84	-0.49(0.10)	0.02	-1.69	-1.46(0.08)	0.013		-0.77	0.18	0.30	0.06
NGC2841	19.5	37.6	2.46	-0.126(0.025)	0.005	0.32	-1.78(0.06)	0.03	-1.88	-1.19(0.05)	0.010		-1.59	0.03	0.57	0.05
NGC1167	24.3	50.4	2.57	-0.146(0.017)	0.019	0.29	-1.45(0.14)	0.05	-1.58	-1.71(0.12)	0.016		-1.85	0.27	0.86	0.08
Toy model	7.7	21.5	2.13	0.131(0.006)	0.005	0.63	-1.71(0.05)	0.03	-1.57	-1.00(0.04)	0.003		-1.62	0.07	0.75	0.09

Columns: (1) gives the galaxy name; (2) and (3) give the radii in kpc enclosing 25% and 75% of the H I mass respectively; columns (4)-(6) relate to the power law fits to the rotation curves - (4) gives the zeropoint, (5) the power-law index, and (6) the dispersion of the residuals in dex; columns (7)-(9) relate to the power law fits to the  $\Sigma_g$  (ISM surface mass density) profiles, with the individual columns following the pattern of (4)-(6); columns (10)-(12) relate to the power law fits to the  $\kappa$  (epicyclic frequency) profiles, with the individual columns following the pattern of (4)-(6); columns (13) and (14) give the average logarithm of  $\zeta$  (local gas fraction) between  $R_1$  and  $R_2$  and its dispersion, respectively; columns (15) and (16) give the average logarithm of  $Q$  (disk stability parameter) between  $R_1$  and  $R_2$  and its dispersion, respectively. Values in parenthesis are the formal uncertainties in the power law slopes from the fits to the relevant profiles.